Chemical Science

EDGE ARTICLE

View Article Online
View Journal | View Issue

Cite this: *Chem. Sci.*, 2019, **10**, 1786

All publication charges for this article have been paid for by the Royal Society of Chemistry

Received 31st October 2018
Accepted 30th November 2018

DOI: 10.1039/c8sc04868a

rsc.li/chemical-science

Oxygen transfer in electrophilic epoxidation probed by ^{17}O NMR: differentiating between oxidants and role of spectator metal oxo†

Christian Ehinger, ‡ Christopher P. Gordon ‡ and Christophe Copéret *

Peroxide compounds are used both in laboratory and industrial processes for the electrophilic epoxidation of olefins. Using NMR-spectroscopy, we investigate why certain peroxides engage in this type of reaction while others require activation by metal catalysts, *e.g.* methyltrioxorhenium (MTO). More precisely, an analysis of ^{17}O NMR chemical shift and quadrupolar coupling parameters provides insights into the relative energy of specific frontier molecular orbitals relevant for reactivity. For organic peroxides or H_2O_2 a large deshielding is indicative of an energetically high-lying lone-pair on oxygen in combination with a low-lying σ*(O–O) orbital. This feature is particularly pronounced in species that engage in electrophilic epoxidation, such as peracids or dimethyldioxirane (DMDO), and much less pronounced in unreactive peroxides such as H_2O_2 and ROOH, which can however be activated by transition-metal catalysts. In fact, for the proposed active peroxo species in MTO-catalyzed electrophilic epoxidation with H_2O_2 an analysis of the ^{17}O NMR chemical shift highlights specific π- and δ-type orbital interactions between the so-called metal spectator oxo and the peroxo moieties that raise the energy of the high-lying lone-pair on oxygen, thus increasing the reactivity of the peroxo species.

Introduction

Electrophilic epoxidations are at the core of numerous processes, ranging from the industrial synthesis of propylene oxide to enzymatic oxygenase reactions.[1–8] In organic synthesis, this ubiquitous transformation is commonly achieved by using stoichiometric epoxidation agents such as *meta*-chloroperoxybenzoic acid (*m*CPBA), dimethyldioxirane (DMDO), or oxaziridines.[9–14] H_2O_2 and ROOH can also be used for epoxidation but they require a catalyst. The most commonly used catalysts are (i) organorhenium trioxides (especially methyltrioxorhenium, MTO)[15–21] and group 6 metal dioxo compounds[22–24] (Fig. 1) or (ii) early transition-metal alkoxides (*e.g.* Ti and V),[25–29] that involve peroxo-species as key reaction intermediates.

While the reactivity of oxidizing agents such as *m*CPBA or DMDO towards olefins is well established and exploited synthetically, the origin of their reactivity towards C–C double bonds has not been studied in detail. This question is particularly apparent when considering that other peroxides, such as H_2O_2 or *t*BuOOH, are usually not reactive towards olefins, unless combined with metal catalysts.

Recent work has shown that analysis of the ^{13}C NMR chemical shift tensor (CST) of metal alkyl compounds can give valuable insights into the electronic structure and the reactivity of ubiquitous reaction intermediates in organometallic chemistry and homogeneous catalysis.[30–37] Considering the large chemical shift window of ^{17}O nuclei (around 1200 ppm), we reasoned that analysis of the ^{17}O NMR chemical shift tensor of oxidants would allow for a detailed understanding of the electronic structure and associated reactivity of these molecules. In addition, the quadrupolar coupling constant of ^{17}O (nuclear spin $I = 5/2$) can provide valuable information on the charge distribution around the nucleus.[38–42] In fact, ^{17}O NMR

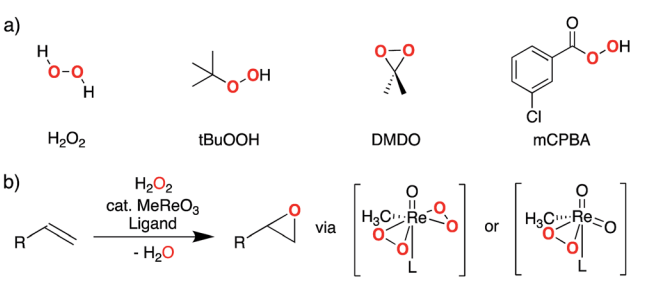

Fig. 1 (a) Representative primary peroxide oxidants used for electrophilic epoxidation, (b) MTO-catalyzed olefin epoxidation involving bisperoxo- or monoperoxo-species (L = pyridine or water).

Department of Chemistry and Applied Biosciences, ETH Zürich, Vladimir Prelog Weg 1-5, 8093, Zürich, Switzerland. E-mail: ccoperet@ethz.ch

† Electronic supplementary information (ESI) available: Computational details, calculated chemical shift tensors and quadrupolar coupling parameters, complete results of NCS analysis, visualizations of relevant NLMOs, graphical representations of chemical shift and EFG tensors, experimentally measured NMR spectra and corresponding simulations, coordinates of all computed structures. See DOI: 10.1039/c8sc04868a

‡ These authors contributed equally to this work.

spectroscopy has been used to identify and study peroxo species as well as related compounds containing O–N bonds.[43–46]

The isotropic chemical shift δ_{iso} (eqn (1)) and the three principal components ($\delta_{11} \geq \delta_{22} \geq \delta_{33}$) of the CST contain a considerable amount of information on the electronic structure of NMR active nuclei. The corresponding shielding values (σ, eqn (2)), can be decomposed computationally into diamagnetic (σ_{dia}) and paramagnetic contributions, which also include contributions from spin–orbit coupling ($\sigma_{para+SO}$, eqn (3)). While the diamagnetic contributions, which arise from a molecule's electronic ground state, lead to shielding and are usually similar for all nuclei of a given kind independent of their chemical environment, the paramagnetic contributions, which give mostly rise to deshielding, originate from magnetically induced coupling of excited states to the ground state, by action of the angular momentum operator $\hat{\boldsymbol{L}}_i$, as described in a 2nd order perturbation approach in eqn (4).[47]

$$\delta_{iso} = \frac{1}{3}(\delta_{11} + \delta_{22} + \delta_{33}) \quad (1)$$

$$\delta_{ii} = \sigma_{iso}^{ref} - \sigma_{ii} \quad (i = 1, 2, 3) \quad (2)$$

$$\sigma = \sigma_{dia} + \sigma_{para+SO} \quad (3)$$

$$\sigma_{ii,para} \Leftrightarrow -\frac{\left\langle \Psi_{occ} \middle| \hat{L}_i \middle| \Psi_{vac} \right\rangle \left\langle \Psi_{vac} \middle| \hat{L}_i / r^3 \middle| \Psi_{occ} \right\rangle}{\Delta E_{vac-occ}} \quad (4)$$

According to eqn (4), deshielding of a nucleus is expected along the direction i, if an occupied orbital on this nucleus can be "superimposed" onto a vacant orbital on the same nucleus rotated by 90° along the axis i (Fig. 2). Since the extent of deshielding increases with a decreasing energy gap between the two orbitals, the paramagnetic contribution to shielding is most strongly affected by frontier molecular orbitals (FMOs) – energetically high-lying occupied and low-lying vacant orbitals.

In this work, we make use of chemical shift to evidence specific high-lying occupied and low-lying vacant orbitals in the aforementioned oxidizing agents, thereby probing their electronic structure and connection to the observed reactivities.

As ^{17}O is a quadrupolar nucleus ($I = 5/2$), the quadrupolar coupling, which typically complicates the interpretation of spectra by line broadening, holds information about the distribution of charges around the nucleus. The quadrupolar interaction is proportional to the electric field gradient (EFG) tensor $\ddot{V}$ (eqn (5)), where e is the electron charge, Q is the quadrupolar moment of ^{17}O, $\hbar$ is the reduced Planck constant ($\hbar = h/2\pi$), $\hat{\boldsymbol{I}}$ is the nuclear spin operator and I the nuclear spin quantum number.

$$\hat{\boldsymbol{H}}_Q = \frac{eQ}{2I(2I-1)\hbar} \hat{\boldsymbol{I}} \ddot{\boldsymbol{V}} \hat{\boldsymbol{I}} \quad (5)$$

V is a traceless second rank tensor ($\boldsymbol{V_{11}} + \boldsymbol{V_{22}} + \boldsymbol{V_{33}} = 0$) where we follow the notation $|\boldsymbol{V_{33}}| \geq |\boldsymbol{V_{22}}| \geq |\boldsymbol{V_{11}}|$ for the three principal components. The EFG tensor can be described by two independent variables – usually the largest principal component ($\boldsymbol{V_{33}}$) and the asymmetry parameter $\boldsymbol{\eta_Q}$ (eqn (6)).

$$\boldsymbol{\eta_Q} = (\boldsymbol{V_{11}} - \boldsymbol{V_{22}})/\boldsymbol{V_{33}} \quad (6)$$

The quadrupolar coupling constant $\boldsymbol{C_Q}$ arises from the interaction of the quadrupole moment of ^{17}O ($I = 5/2$) with the EFG and is proportional to $\boldsymbol{V_{33}}$ (eqn (7)).[38] Since the electric quadrupole moment Q of the ^{17}O nucleus is negative, $\boldsymbol{V_{33}}$ and $\boldsymbol{C_Q}$ have opposing signs.

$$\boldsymbol{C_Q} = (eQ\boldsymbol{V_{33}}/h) \quad (7)$$

$\boldsymbol{V_{33}}$ and hence $\boldsymbol{C_Q}$ are indicative of how symmetric the EFG and thus the charge distribution around the nucleus is. This has been a valuable tool to assess local symmetry around quadrupolar nuclei (*e.g.* ^{17}O, ^{27}Al, ^{45}Sc).[38,41,42,46,48–51]

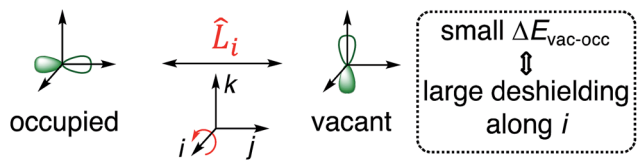

Fig. 2 Magnetically induced coupling of occupied and vacant orbitals leading to a deshielding along the i-axis.

Results & discussion

CSTs of non-metal-based peroxides

We calculated the chemical shift tensors (CSTs) of selected peroxides relevant to epoxidation reactions, as well as associated reduced compounds. We chose to investigate DMDO and *m*CPBA, two compounds showing activity towards electrophilic epoxidation, as well as H_2O_2 and *t*BuOOH that do not participate in this transformation, unless activated by metal catalysts. In order to benchmark our calculations, we also experimentally determined the ^{17}O NMR chemical shift tensors of H_2O_2[52] and acetone by solid-state ^{17}O NMR spectroscopy[53–55] (see ESI† for experimental details).

The measured and calculated chemical shifts are given in Table 1. Generally, a good agreement between calculated and experimental data (when available) is obtained. The oxygen atoms of the unsymmetric peroxides (*t*BuOOH and *m*CPBA) are labelled (O), for the oxygen bound to a carbon atom and (OH) for the oxygen connected to the hydrogen.

A comparison of the isotropic chemical shifts given in Table 1 reveals that all peroxide species (H_2O_2, *t*BuOOH, *m*CPBA, and DMDO) show significantly more deshielded δ_{iso} values in comparison with H_2O, *t*BuOH and *m*CBA, albeit less deshielded than carbonyl oxygens (*e.g.* mCBA (C=O) and acetone). While the differences among the various peroxides are less pronounced, the chemical shift (δ_{iso}) of the oxygen atom which is transferred during epoxidation reactions is more deshielded for DMDO and *m*CPBA (OH) as compared to H_2O_2 and *t*BuOOH (OH). A closer inspection of the principal components of the chemical shift tensor reveals that this is mostly due to the δ_{11}

Table 1 Calculated chemical shift tensor parameters of the investigated peroxides and their respective reduced compounds: H_2O, *t*BuOH, *meta*-chlorobenzoic acid and acetone. Where available, experimental values are given in parenthesis (all values in ppm). All calculated shifts are referenced with respect to H_2O

Compound	δ_{iso}	δ_{11}	δ_{22}	δ_{33}	Ω^a
H_2O_2	195 (195)[b]	364 (362)	227 (232)	−7 (−9)	371 (370)
H_2O	0 (0)	25	8	−32	57
*t*BuOOH (O)	273 (246)[56]	413	335	73	340
*t*BuOOH (OH)	205 (206)[56]	386	228	2	384
*t*BuOH	95 (62)[57]	130	104	52	78
*m*CPBA (O)	308 (320)[58]	428	261	236	192
*m*CPBA (OH)	278 (275)[58]	540	245	50	490
*m*CBA (C=O)	398	618	535	42	576
*m*CBA (OH)	193	342	161	76	266
DMDO	291 (302)[59]	636	164	73	564
Acetone	667 (625)[b]	1239 (1185)	740 (705)	23 (−15)	1216 (1200)

[a] $\Omega = \delta_{11} - \delta_{33}$. [b] Note that the quadrupolar nature of ^{17}O can lead to inaccuracies in the determination of the chemical shift tensors – see ESI for a more detailed discussion of the experimental measurements. Additionally, the presence of solvents can also significantly impact the chemical shift.

component of the CST which is significantly more deshielded in DMDO and the OH–oxygen of *m*CPBA (636 and 540 ppm) than in H_2O_2 and *t*BuOOH (364 and 386 ppm). This highly deshielded component is accompanied by a significantly larger span Ω of the CST in the former compounds.

Orientation of the CSTs

In order to further understand these observed trends, we investigated the orientation of the ^{17}O NMR chemical shielding tensors (CSTs) as obtained by DFT calculations. The calculated CSTs are shown in Fig. 3. Notably, the ^{17}O CST is similarly oriented in all the aforementioned peroxides, with the most deshielded δ_{11} component being oriented perpendicular to the O–O axis and lying in the O–O–H/R plane. The δ_{33} component points along the O–O axis, while δ_{22} is perpendicular to both, δ_{11} and δ_{33}. Minor deviations to this pattern are found for *m*CPBA (O) and DMDO, where the orientation of the δ_{11} and δ_{33} components is slightly tilted, by comparison with the other compounds (*vide infra*).

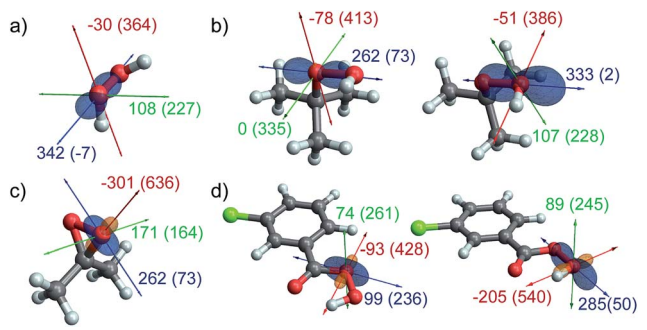

Fig. 3 Orientation of the CST in (a) H_2O_2, (b) *t*BuOOH, (c) DMDO, and (d) *m*CPBA. The principal components σ_{11}, σ_{22}, and σ_{33} are indicated by red, green, and blue arrows, respectively. The ^{17}O NMR shielding values (σ) are indicated in ppm next to the direction of each principal component, with the corresponding chemical shift values (δ) given in parenthesis.

Orbital analysis of the CSTs

We decided to further elucidate the origin of deshielding in the individual components of the CST in a Natural Chemical Shielding (NCS) analysis.[47,48,60–65] This analysis allows for a decomposition of the σ_{ii}/δ_{ii} components into diamagnetic (σ_{dia}) and paramagnetic/spin–orbit ($\sigma_{para+SO}$) contributions (eqn (3)). The paramagnetic term can then be further decomposed into contributions of the various NLMOs (bonds and lone pairs) surrounding the nucleus of interest. Due to the orbital energy difference in the denominator of eqn (4), the orbitals contributing most strongly to $\sigma_{para+SO}$ are the frontier molecular orbitals (FMOs) of the molecule with a non-vanishing coefficient on the investigated nucleus.

Since the largest differences in the CST of the investigated peroxides originate from the σ_{11}/δ_{11} component of the CST, its orbital analysis will be further discussed (see Fig. S3 and S4† for other components).

The NCS analysis of the σ_{11} component of the various compounds (Fig. 4b) reveals, that the diamagnetic contributions to this component are essentially invariant throughout the whole series of compounds. The differences in δ_{11} result from the paramagnetic contributions, which are mainly affected by four different Natural Localized Molecular Orbitals (NLMOs). These correspond to two lone-pairs on oxygen (denoted as LP 'p' and LP 's'), as well as the two σ-bonding orbitals (denoted as σ(O–R) and σ(O–O)). These four NLMOs are visualized for the case of hydrogen peroxide in Fig. 4a; for the other compounds they are shown in Fig. S11–S13.†

Notably, the dominant contribution to the deshielding of σ_{11}/δ_{11} originates from the LP 'p' on oxygen in all cases given in Fig. 4, with the exception of *m*CPBA (O) (*vide infra*). The observation of the large deshielding perpendicular to the O–O axis originating from this lone pair indicates the presence of a low-lying vacant orbital, oriented perpendicular to both the lone-pair and the direction of σ_{11}/δ_{11}; *i.e.* oriented along the O–O bond (eqn (4)). This vacant orbital corresponds to σ*(O–O), the lowest unoccupied molecular orbital with contribution of oxygen in all of the investigated peroxides. As the extent of

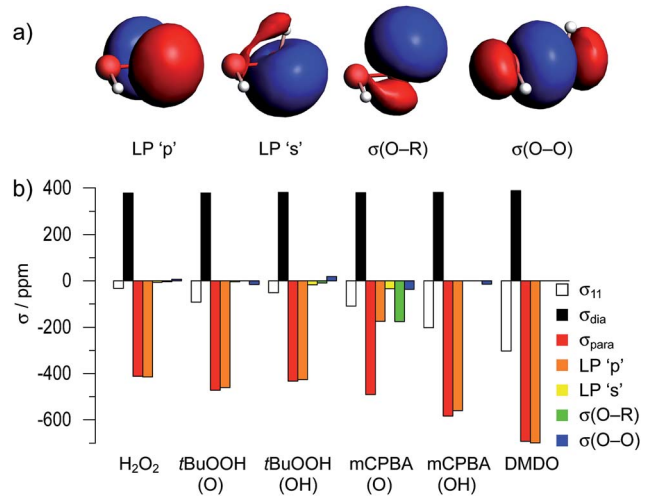

Fig. 4 (a) Relevant NLMOs contributing to the paramagnetic shielding of the investigated peroxides. (b) Results of the NCS analysis of the most deshielded component of the shielding tensor, σ_{11}, represented in a bar diagram.

deshielding along a CST principal axis scales with the inverse of the energy difference between the two coupled orbitals (eqn (4)), a large deshielding of the δ_{11} component indicates the presence of a high-lying LP 'p' on oxygen, derived from the filled bonding and antibonding π(O–O) and π*(O–O) orbitals, and/or a low-lying σ*(O–O) orbital. The comparatively small contribution of the LP 'p' to δ_{11} in the case of the oxygen bound to the carbonyl group in *m*CPBA, which is associated with a different orientation of this component compared to the other compounds (Fig. 3), can be rationalized by the conjugation to the carbonyl group, which decreases the energy of the lone pair LP 'p' and thus renders the coupling to the σ*(O–O) less efficient. Additionally, this conjugation leads to a non-zero coefficient of a vacant orbital with π-symmetry on the oxygen. The C–O σ-bond can couple to this vacant orbital, ultimately leading to the significant contribution of the NLMO σ(O–R) and the tilting of the CST component δ_{11}. In the case of DMDO the slightly tilted orientation of the CST is rationalized by the deviation of the electron density from the internuclear axis in this strained system. This bonding situation can be understood by Walsh-type orbitals ("banana bonds").[66] The tilting of the CST hence evidences the deviation of the σ*(O–O) orbital from the O–O axis. This is consistent with the result of the Natural Hybrid Orbital (NHO) Directionality and Bond Bending Analysis which indicates a deviation of the localized orbital from the internuclear (O–O) axis by 16.8°, as opposed to 2.5° in the case of H_2O_2 (the values for other investigated compound are given in Table S6†).[67]

Energetic considerations in oxygen-transfer reactions

The strong deshielding of the δ_{11} component in the case of DMDO and *m*CPBA evidences a particularly low-lying σ*(O–O) orbital in combination with a high-lying lone pair LP 'p' in these compounds. In order to further understand the impact of this orbital situation on reactivity we investigated the corresponding transition states for the epoxidation of ethylene with DMDO and *m*CPBA. In both transition states, the olefin is oriented perpendicularly to the plane consisting of the peroxo moiety and the respective substituents (Fig. 5). The free energies of activation for DMDO and *m*CPBA are found at 25.6 and 25.7 kcal mol^{-1}, respectively.

The geometry of these transition states can be rationalized by the orbital situation derived from the CST analysis: while a low-lying σ*(O–O) orbital of the peroxide allows for a good interaction with the π(C=C) bond of the olefin, the oxygen lone pair LP 'p' involved in the filled π*(O–O) orbital can interact with the empty π*(C=C) orbital (Fig. 6). Both of these interactions are energetically favorable and are expected to lower the transition state energy for olefin epoxidation. The deshielded δ_{11} component of the CST is thus indicative of the epoxidation propensity of DMDO and *m*CPBA.

The ^{17}O NMR chemical shift of the investigated peroxides shows that DMDO and *m*CPBA, the two molecules engaging in electrophilic epoxidation, feature a high-lying lone pair LP 'p' and a low-lying σ*(O–O) orbital. This observation can be understood based on the geometry of these compounds: In DMDO and *m*CPBA the lone pairs LP 'p' of the peroxo oxygens are co-planar, resulting in a maximized filled–filled interaction (α-effect), and thus a high-lying filled antibonding π*(O–O) orbital. Hence, in the epoxidation process, the backdonation of the lone pair of the attacked oxygen into the π*(C=C) of the olefin is more efficient for these reagents.

The importance of this "backdonation" was further explored by investigating transition state geometries where the olefin is perpendicular to the oxygen lone pair and hence co-planar with the dioxirane moiety in DMDO or the carbonyl group in *m*CPBA. The corresponding transition state (2nd order saddle point) energies for the epoxidation where the rotation around the reaction coordinate was restricted were found at 32.7 and 29.0 kcal mol^{-1} for DMDO and *m*CPBA, respectively. The

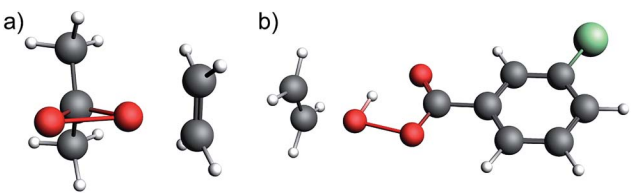

Fig. 5 Transition state geometries for the electrophilic epoxidation with (a) DMDO and (b) *m*CPBA.

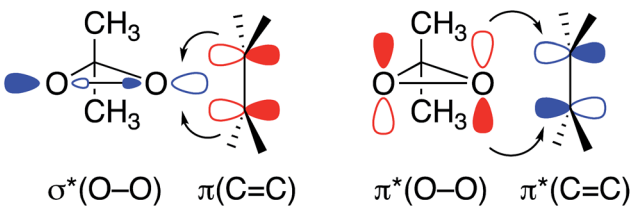

Fig. 6 Relevant orbital interactions in epoxidation, shown for the case of DMDO. Electron-donating and -accepting orbitals are colored in red and blue, respectively.

backdonation of the LP 'p' into the π*(C=C) of the olefin hence gives rise to a significant stabilization of the transition state energy in both cases (7.1 kcal mol^{-1} for DMDO and 3.3 kcal mol^{-1} for *m*CPBA).

Quadrupolar coupling parameters

To complement the analysis of the ^{17}O NMR parameters we calculated the quadrupolar coupling parameters of the aforementioned peroxides. The respective ^{17}O C_Q and η_Q-values are reported in Table 2.

For all investigated peroxide oxygens, the absolute magnitude of the quadrupolar coupling constant C_Q (and V_{33} accordingly) is significantly larger than for water. The orientation of the EFG tensor is similar in all of these peroxides, with the most positive component oriented along the O–O bond, and the most negative component oriented in the direction of LP 'p' (selected examples in Fig. 7a–c, see Fig. S14† for other compounds). This orientation is hence indicative of a region of high electron density in the direction of LP 'p', and a region of depleted electron density in the direction of the O–O bond. The reversed sign of C_Q observed for DMDO in contrast to other peroxides is due to the definition of V_{33}, which always corresponds to the EFG tensor component with the largest absolute value (indicated by a red arrow in Fig. 7). While the EFG tensor is similar in all peroxides, the negative EFG tensor component perpendicular to the O–O bond is slightly larger for DMDO by absolute value as compared to the positive EFG tensor component along the O–O bond. For the other investigated peroxides, the situation is reversed, leading to a change in sign of V_{33} and hence of C_Q. The large C_Q value for peroxides in combination with the specific orientation of the EFG tensor is consistent with the presence of a high-lying occupied orbital (LP 'p') oriented perpendicular to a low-lying vacant σ*(O–O) orbital in these species. This observation parallels what is seen from the NCS analysis of the δ_{11} component of the CST.

Table 2 Calculated ^{17}O quadrupolar coupling parameters. Experimentally measured values are given in parenthesis

Compound	C_Q [MHz]	η_Q
H_2O	10.3	0.78
H_2O_2	−17.0 (−16)	0.93 (0.8)
*t*BuOOH (O)	−17.5	0.95
*t*BuOOH (OH)	−16.1	0.97
*m*CPBA (O)	−14.4	0.54
*m*CPBA (OH)	−18.8	0.75
DMDO	18.5	0.79
Acetone	11.8 (12)	0.52 (0.6)

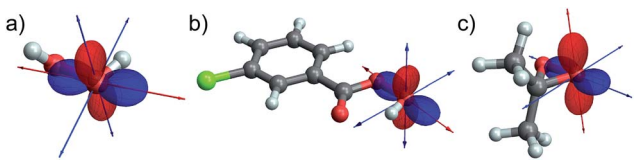

Fig. 7 EFG-tensor orientations of (a) H_2O_2, (b) *m*CPBA (OH), and (c) DMDO. Negative regions of the EFG tensor are represented in red, positive regions are depicted in blue. The direction of V_{33} is indicated with a red arrow.

MTO-catalyzed epoxidation

As both H_2O_2 and *t*BuOOH are inactive in electrophilic epoxidation but are rendered active in the presence of transition-metal catalysts, we investigated the process of activation and the properties of the proposed active species. We chose methyltrioxorhenium (MTO) as a prototypical catalyst because of its high efficiency in olefin epoxidation with H_2O_2 (Fig. 1b), and the existence of detailed mechanistic studies (isolation of reaction intermediates, measurements of ^{17}O NMR parameters and computational studies).[15,68–71] We hence calculated the chemical shift tensors of MTO (Table 3 and Fig. 8c) and of the water and pyridine adducts of the corresponding mono- and bisperoxides (Table 3). The bisperoxo pyridine adduct will be discussed in more detail; the tensors are shown in Fig. 8a and b.[17–19,72] The CSTs and NCS analyses for other intermediates are provided in the ESI† (Table S1, Fig. S1 and Tables S2–S4, Fig. S8–S10,† respectively) and further commented below for comparison.

CST of peroxo intermediates

The measured and calculated chemical shifts of bis- and monoperoxo intermediates of the MTO-catalyzed olefin epoxidation are given in Table 3. Both the isotropic chemical shift (δ_{iso}) and the three principal components of the CST are significantly more deshielded in the metal-peroxide compound by comparison with H_2O_2 (Table 3, where *cis*/*trans* denotes the peroxo oxygen pseudo-*cis*/*trans* with respect to the methyl substituent). This observation suggests a change in the electronic structure of the peroxide oxygen atoms, which is likely connected to their increased reactivity towards olefins. Note the significantly larger deshielding found for the oxo-ligands as typically observed for metal-oxo compounds.[73,74] The CSTs of the peroxo oxygen atoms have similar orientations as shown in Fig. 8 (and Fig. S1† for the water adducts and the monoperoxo species). For both peroxo oxygens, σ_{11}/δ_{11} and σ_{22}/δ_{22} are in the O–Re–O plane (defined by Re and the two peroxo O-atoms) whereas σ_{33}/δ_{33} is perpendicular to it. In contrast to H_2O_2, the most deshielded component of the metal peroxo species, δ_{11}, is no longer oriented perpendicularly to the O–O axis but is significantly tilted, while remaining in the peroxo O–Re–O plane. One can also note differences of chemical shifts observed for the *cis* and *trans* peroxo oxygens in the bisperoxo compounds, the former being slightly more deshielded than the latter for both δ_{iso} and δ_{11}. These values are not strongly affected by the apical ligand (pyridine *vs.* water), suggesting a similar electronic structure in all bisperoxo intermediates. For the monoperoxo species, the δ_{iso} of both peroxo oxygens are more similar, albeit slightly more deshielded than in the bisperoxo intermediates.

Orbital analysis of the CSTs

An orbital analysis reveals that the largest contribution to the paramagnetic deshielding of the σ_{11}/δ_{11} component arises from

Table 3 Calculated ^{17}O chemical shift tensors and C_Q values of H_2O_2, MTO and the corresponding bisperoxo- and monoperoxo-species; *cis*/*trans* denotes the peroxo oxygen pseudo-*cis*/*trans* to the methyl substituent; L = pyridine. Experimental values are given in parenthesis[68,70] (chemical shift values are given in ppm and referenced with respect to H_2O, C_Q values are given in MHz)

Compound	δ_{iso}	δ_{11}	δ_{22}	δ_{33}	Ω^a	C_Q
MTO	894 (820)	1392 (1326)	718 (629)	571 (506)	821 (820)	−4.6 (−4)
$MeReO(O_2)_2L$ *cis*	416	563	358	326	237	−15.0
$MeReO(O_2)_2L$ *trans*	378	528	406	201	328	−15.2
$MeReO(O_2)_2(OH_2)$ *cis*	422 (422)[68]	572	365	329	243	−15.0
$MeReO(O_2)_2(OH_2)$ *trans*	364 (363)[68]	507	394	192	315	−15.0
$MeReO_2(O_2)L$ *cis*	419	565	380	312	253	−17.2
$MeReO_2(O_2)L$ *trans*	425	695	357	221	474	−13.0
$MeReO_2(O_2)$ *cis*[b]	437	602	374	336	266	−16.2
$MeReO_2(O_2)$ *trans*[b]	405	646	335	235	411	−13.3
H_2O_2[c]	195 (195)	364 (362)	227 (232)	−7 (−9)	371 (370)	−17.0 (−16)

[a] $\Omega = \delta_{11} - \delta_{33}$. [b] The monoperoxo species is proposed not to coordinate an additional water-ligand; in fact, coordination of water has little effect on the NMR parameters and the water-ligand dissociated upon optimizing the O-transfer transition state.[75] [c] Same data as shown in Table 1.

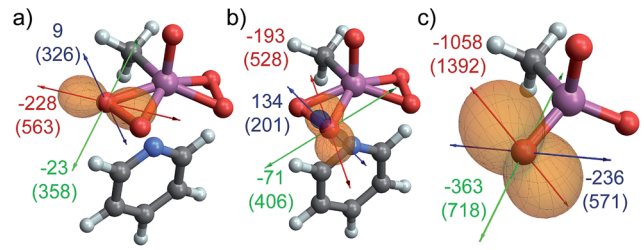

Fig. 8 Chemical shielding tensor orientation in (a) $MeReO(O_2)_2L$ *cis*, (b) $MeReO(O_2)_2L$ *trans* and (c) MTO. The direction of the principal components σ_{11}, σ_{22}, and σ_{33} are indicated by red, green, and blue arrows, respectively. The chemical shielding values (σ) are indicated next to each principal component, with the corresponding chemical shift values (δ) given in parenthesis.

the LP 'p', as was also observed for non-metal-based peroxides (shown in Fig. 9 for the bisperoxo pyridine adduct). Note however, that a significant contribution of the σ(O–Re) bond is also observed for the metal-peroxo species. The other components and peroxo species are given in Tables S2–S4 and Fig. S6–S10.†

While the contributions of the LP 'p' is again indicative of a low-lying σ*(O–O) orbital in combination with high-lying lone-pairs LP 'p' on oxygen, the significant contribution of the σ(O–Re) bond to σ_{11}/δ_{11} evidences the presence of a low-lying vacant orbital perpendicular to the O–Re–O plane with oxygen-contribution. A closer inspection reveals that the bonding combination of the oxygen lone pairs LP 'p' perpendicular to the O–Re–O plane – π(O–O) – can interact with an empty metal d-orbital (*i.e.* d_{yz}) forming a π-bond while the anti-bonding combination of the LP 'p' – π*(O–O) – can interact with another empty d-orbital (*i.e.* d_{xz}) in a δ type fashion (Fig. 10). In fact, the calculated molecular orbitals suggest that the anti-bonding combinations of the above mentioned δ- and π-bonds are the LUMO and LUMO+1 of the MTO bisperoxide, respectively.

As observed for non-metal-based peroxides, the MTO-derived bisperoxide shows rather large C_Q values (−15.0 MHz and −15.2 MHz for the *cis*- and *trans*-oxygen, respectively, see Table S5 and Fig. S15†) by comparison with MTO (−4.6 MHz). This again indicates a large electric field gradient around the peroxide O-atoms, consistent with a high-lying lone pair oriented

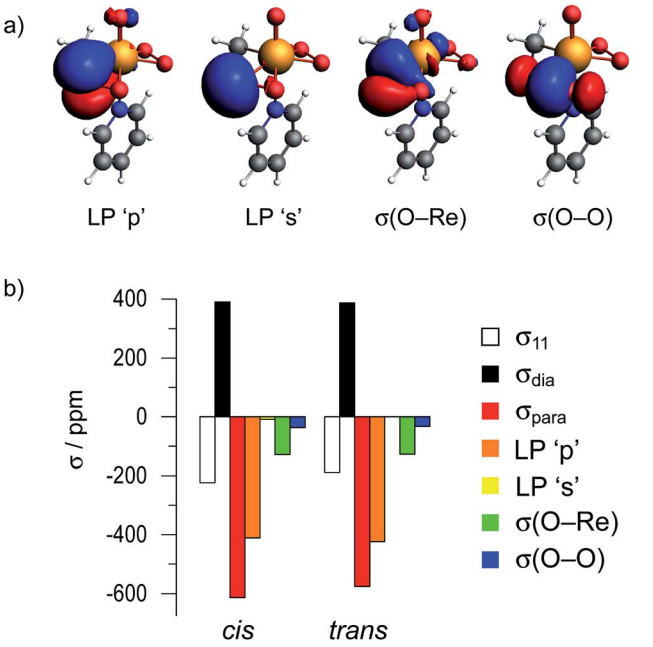

Fig. 9 (a) Orbitals with a significant contribution to the paramagnetic shielding shown for the case of the oxygen pseudo-*cis* to the methyl group. (b) NCS analysis of the most deshielded component of the CST, σ_{11}, for both peroxo oxygens.

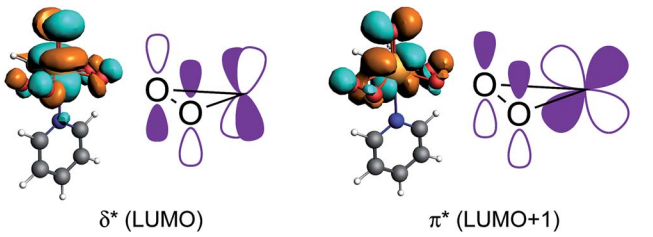

Fig. 10 δ*- and π*-orbitals, which were found to be the LUMO and LUMO+1 of the MTO bisperoxide.

perpendicularly to a low-lying σ*(O–O) orbital. As observed for the CST, also the C_Q values of the peroxo oxygen atoms are rather insensitive towards replacement of the pyridine ligand by water; the corresponding water adduct shows a C_Q of −15.0 MHz on both oxygen atoms. These values differ more in the monoperoxo species, where C_Q's are equal to −17.2 and −13.0 MHz for the *cis*- and *trans*-oxygen in the pyridine adduct, respectively, consistent with a more dissymmetric structure (Table 3).

Energetic considerations in oxygen-transfer reactions

Transition state energy calculations were performed both for the attack of ethylene at the oxygen pseudo-*cis* to the methyl group and the oxygen pseudo-*trans* to it. The obtained geometries for the bis-peroxo pyridine adducts are shown in Fig. 11 (others are given as coordinate files in the ESI†).

The free energy barriers from the bis-peroxo pyridine adduct are 34.2 kcal mol^{-1} and 27.2 kcal mol^{-1} for transfer of the *cis* and *trans* oxygens, respectively. Notably, the more deshielded oxygen atom (pseudo-*cis* to the methyl ligand) is associated with a less favorable oxygen transfer step, consistent with a CST already close to what is observed in metal-oxo species, showing the connection between reactant and product. While in H_2O_2 the dihedral angle (H–O–O–H) is calculated to be 114° with the two LP 'p' on the oxygen pointing away from each other, the lone pairs are coplanar in a peroxo metal complex, introducing again a maximized α-effect (similar to DMDO and *m*CPBA). In order to understand and quantify the effect of the LP 'p' back-donation into the olefin π*-orbital to the transition state energy, and hence probe the importance of the α-effect, a transition state (2nd order saddle point), where the attacking olefin is coplanar with the peroxo O–Re–O plane was calculated for the case of the oxygen pseudo-*trans* to the methyl group. The obtained free energy of activation was found to be at 31.6 kcal mol^{-1} and thus 4.4 kcal mol^{-1} higher in energy than for the perpendicular transition state. This is consistent with what has been found for the epoxidation with non-metal-based peroxides, again evidencing the importance of the back-donation of a high-lying LP 'p' on oxygen – the filled π*(O–O) orbital – into the olefin π*(C=C) orbital.

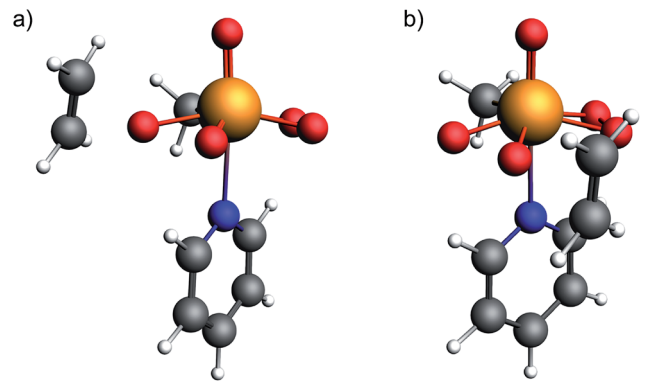

Fig. 11 Optimized transition state geometries for the epoxidation of ethylene with the bisperoxide of MTO, for the attack at the oxygen (a) pseudo-*cis* and (b) pseudo-*trans* to the methyl group.

Similar trends are observed for the bis-peroxo water adduct with free energy barriers of 34.3 and 27.8 kcal mol^{-1}, for the transfer of the *cis*- and *trans*-oxygen, respectively. For the mono-peroxo intermediate, the free energy barriers for O-transfer are typically slightly higher (>29.0 kcal mol^{-1}) for both oxygen atoms, at the exception of the *cis*-peroxo oxygen of the pyridine adduct (26.8 kcal mol^{-1}). These results suggest that the bis-peroxo complex is possibly the more reactive species in water, and that in the presence of pyridine both mono- and bis-peroxo complexes are reactive.[72,75] Thus pyridine may have a dual role, *i.e.* as a phase transfer agent and as a ligand to accelerate catalysis.[17,76] Notably, for all metal-peroxo compounds, the easier oxygen transfer is associated with the peroxo oxygen with smaller δ_{iso} and δ_{11}, while the oxygen atom which is not transferred displays a larger oxo-character, evidenced by the larger δ_{iso} and δ_{11}.

As for DMDO and *m*CPBA, the coplanarity of the two oxygen lone pairs LP 'p' in the MTO peroxo species maximizes the α-effect, raising the energy of the lone pairs thereby increasing their reactivity. In addition, the π-interaction of the peroxo moiety with the metal (Fig. 10) assists the oxygen transfer process in olefin epoxidation, during which a fully developed π(Re=O) bond is formed.

Notably, the spectator oxo-ligand in the apical position in the bisperoxo Re complex is not innocent: this oxo-ligand interacts with the peroxo moiety *via* the metal d-orbitals involved in the π- and δ-interactions (Fig. 10). This interaction minimizes the stabilization of the peroxo LP 'p' by weakening the (stabilizing) δ- and π-bonds. In addition, the presence of the spectator oxo-ligand also provides a driving force for the formation of the metal-peroxo species in the catalytic cycle: formation of the peroxo species from MTO strengthens the bond of the apical "spectator" oxo-ligand as evidenced by a slight decrease of the Re=O bond length on going from MTO (1.69 Å) to the monoperoxo (1.68 Å) and then the bisperoxo (1.67 Å) pyridine adducts. This effect is reminiscent of the spectator oxo effect discussed for metallacyclobutane formation from metal alkylidenes during the olefin metathesis reaction, as well as for the formation of metallacycle oxetane intermediates in the reaction of alkenes with metal oxo compounds.[77–79]

Conclusions

Overall, peroxide compounds are associated with significantly deshielded ^{17}O chemical shifts that indicate the presence of low-lying vacant and high-lying occupied orbitals, corresponding to the σ*(O–O) and the lone pairs on oxygens, associated with π(O–O) and π*(O–O), for both metal-based and non-metal-based peroxides. These specific electronic features are particularly pronounced in peroxide species that engage in electrophilic epoxidation reactions (DMDO, *m*CPBA, and MTO bisperoxo), as evidenced by their remarkably large deshielding. This is due to the coplanarity of the oxygen lone-pairs in these peroxides which is induced by their strained cyclic structure or by H-bonding in the case of *m*CPBA. Both maximize overlaps and in fine raises the HOMO (α-effect) and increases reactivity towards electrophilic epoxidation. In metal peroxo species, this

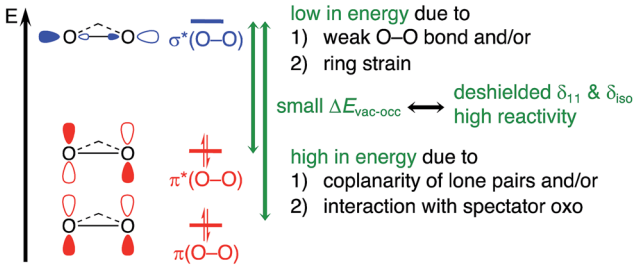

Fig. 12 NMR chemical shift probes specific electronic features with relevance for reactivity in electrophilic epoxidation.

HOMO is further raised in energy by the presence of a spectator oxo-ligand in the apical position. In fact, this "spectator" oxo species participates in modulating the reactivity of peroxo intermediates in transition-metal-catalyzed oxidation processes; it is thus not surprising that such a moiety is ubiquitous in efficient epoxidation catalysts that use H_2O_2 as a primary oxidant. The α-effect and the presence of a strained cyclic structure goes hand in hand with a weakening of the O–O bond. Both the high-lying lone pair of the filled π*(O–O) and the low-lying σ*(O–O) orbital drive the observed reactivity in electrophilic epoxidation, in which these two orbitals interact with the π*(C=C) and π(C=C) orbitals of the olefin, respectively. Thus, ^{17}O NMR chemical shift provides a powerful descriptor to pinpoint key electronic features that are decisive for reactivity in oxidation chemistry (Fig. 12).

Epilogue

The frontier orbital interactions shown in Fig. 6 highlight the following observation: while an epoxidation with DMDO or *m*CPBA is typically thought of as an electrophilic epoxidation, with the oxidant acting as electrophile and the olefin acting as nucleophile, these molecular orbital interactions indicate that both substrates act as nucleophiles and electrophiles by exploiting the low-lying σ*(O–O) orbital and the high-lying lone pair LP 'p' (O) induced by the α-effect. This is reminiscent of synergistic effects observed in transition metal chemistry, for example in olefin complexes or in oxidative addition processes

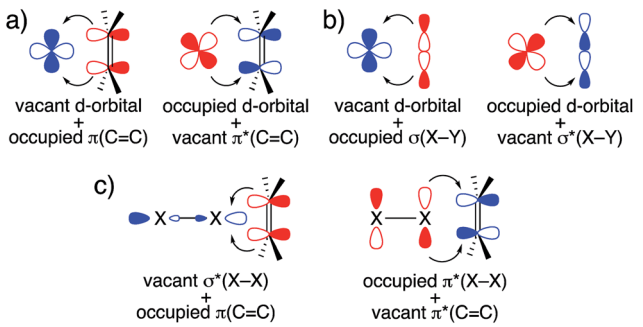

Fig. 13 Relevant synergistic orbital interactions in (a) metal-olefin complexes, (b) oxidative addition processes, and (c) olefin halogenation (X = Cl, Br, I). Electron-donating and -accepting orbitals are colored in red and blue, respectively.

(Fig. 13a and b). Considering that olefin epoxidation with DMDO or *m*CPBA is isolobal to epoxidations with oxaziridines and halogenation reactions by X_2 or NXS (X = Cl, Br, I), a similar orbital picture can be anticipated for these "electrophilic" additions (Fig. 13c).

Conflicts of interest

There are no conflicts to declare.

Acknowledgements

C. P. G is a recipient of the Scholarship Fund of the Swiss Chemical Industry. E. Lam is acknowledged for helpful discussions. K. Yamamoto and W.-C. Liao are acknowledged for the synthesis and the NMR characterization of ^{17}O-labelled H_2O_2, respectively.

Notes and references

1 R. A. Sheldon, *J. Mol. Catal.*, 1980, **7**, 107–126.
2 B. Notari, *Adv. Catal.*, 1996, **41**, 253–334.
3 R. Jira, R. A. Sheldon, P. Lappe, E. Schulz, R. W. Fischer and F. Röhrscheid, in *Applied Homogeneous Catalysis with Organometallic Compounds*, ed. B. Cornils and W. A. Herrmann, Wiley-VCH, Weinheim, 2008.
4 T. A. Nijhuis, M. Makkee, J. A. Moulijn and B. M. Weckhuysen, *Ind. Eng. Chem. Res.*, 2006, **45**, 3447–3459.
5 T. Zhang, L. Mazaud, L.-M. Chamoreau, C. Paris, A. Proust and G. Guillemot, *ACS Catal.*, 2018, **8**, 2330–2342.
6 B. Bühler, K. Bühler and F. Hollman, in *Enzyme Catalysis in Organic Synthesis*, ed. K. Drauz, H.Gröger and O.May, Wiley-VCH, Weinheim, 2012.
7 Y. Liang, J. Wei, X. Qiu and N. Jiao, *Chem. Rev.*, 2018, **118**, 4912–4945.
8 J. Dong, E. Fernández-Fueyo, F. Hollmann, C. E. Paul, M. Pesic, S. Schmidt, Y. Wang, S. Younes and W. Zhang, *Angew. Chem., Int. Ed.*, 2018, **57**, 9238–9261.
9 N. Prileschajew, *Ber. Dtsch. Chem. Ges.*, 1909, **42**, 4811–4815.
10 H. Hussain, A. Al-Harrasi, I. R. Green, I. Ahmed, G. Abbas and N. U. Rehman, *RSC Adv.*, 2014, **4**, 12882–12917.
11 R. W. Murray and R. Jeyaraman, *J. Org. Chem.*, 1985, **50**, 2847–2853.
12 Y. Zhu, Q. Wang, R. G. Cornwall and Y. Shi, *Chem. Rev.*, 2014, **114**, 8199–8256.
13 F. A. Davis and A. C. Sheppard, *Tetrahedron*, 1989, **45**, 5703–5742.
14 K. S. Williamson, D. J. Michaelis and T. P. Yoon, *Chem. Rev.*, 2014, **114**, 8016–8036.
15 W. A. Herrmann, R. W. Fischer, W. Scherer and M. U. Rauch, *Angew. Chem., Int. Ed. Engl.*, 1993, **32**, 1157–1160.
16 W. A. Herrmann, R. W. Fischer, M. U. Rauch and W. Scherer, *J. Mol. Catal.*, 1994, **86**, 243–266.
17 J. Rudolph, K. L. Reddy, J. P. Chiang and K. B. Sharpless, *J. Am. Chem. Soc.*, 1997, **119**, 6189–6190.
18 C. Copéret, H. Adolfsson and K. B. Sharpless, *Chem. Commun.*, 1997, **0**, 1565–1566.

19 H. Adolfsson, C. Copéret, J. P. Chiang and A. K. Yudin, *J. Org. Chem.*, 2000, **65**, 8651–8658.
20 S. Huber, M. Cokoja, M. Drees, J. Mínk and F. E. Kühn, *Catal. Sci. Technol.*, 2013, **3**, 388–393.
21 F. Dyckhoff, S. Li, R. M. Reich, B. J. Hofmann, E. Herdtweck and F. E. Kühn, *Dalton Trans.*, 2018, **47**, 9755–9764.
22 G. B. Payne and P. H. Williams, *J. Org. Chem.*, 1959, **24**, 54–55.
23 C. Venturello and R. D'Aloisio, *J. Org. Chem.*, 1988, **53**, 1553–1557.
24 J. Y. Piquemal, S. Halut and J. M. Brégeault, *Angew. Chem., Int. Ed.*, 1998, **37**, 1146–1149.
25 T. Katsuki and K. B. Sharpless, *J. Am. Chem. Soc.*, 1980, **102**, 5974–5976.
26 T. Itoh, K. Jitsukawa, K. Kaneda and S. Teranishi, *J. Am. Chem. Soc.*, 1979, **101**, 159–169.
27 J. Jarupatrakorn and T. D. Tilley, *J. Am. Chem. Soc.*, 2002, **124**, 8380–8388.
28 Y. Sawada, K. Matsumoto, S. Kondo, H. Watanabe, T. Ozawa, K. Suzuki, B. Saito and T. Katsuki, *Angew. Chem., Int. Ed.*, 2006, **45**, 3478–3480.
29 A. Berkessel, T. Günther, Q. Wang and J.-M. Neudörfl, *Angew. Chem., Int. Ed.*, 2013, **52**, 8467–8471.
30 M. Kaupp, V. G. Malkin, O. L. Malkina and D. R. Salahub, *Chem.–Eur. J.*, 1996, **2**, 24–30.
31 V. H. Gessner, F. Meier, D. Uhrich and M. Kaupp, *Chem.–Eur. J.*, 2013, **19**, 16729–16739.
32 S. Halbert, C. Copéret, C. Raynaud and O. Eisenstein, *J. Am. Chem. Soc.*, 2016, **138**, 2261–2272.
33 D. P. Estes, C. P. Gordon, A. Fedorov, W.-C. Liao, H. Ehrhorn, C. Bittner, M. L. Zier, D. Bockfeld, K. W. Chan, O. Eisenstein, C. Raynaud, M. Tamm and C. Copéret, *J. Am. Chem. Soc.*, 2017, **139**, 17597–17607.
34 C. P. Gordon, K. Yamamoto, W.-C. Liao, F. Allouche, R. A. Andersen, C. Copéret, C. Raynaud and O. Eisenstein, *ACS Cent. Sci.*, 2017, **3**, 759–768.
35 K. Yamamoto, C. P. Gordon, W. C. Liao, C. Copéret, C. Raynaud and O. Eisenstein, *Angew. Chem., Int. Ed.*, 2017, **56**, 10127–10131.
36 C. P. Gordon, K. Yamamoto, K. Searles, S. Shirase, R. A. Andersen, O. Eisenstein and C. Copéret, *Chem. Sci.*, 2018, **9**, 1912–1918.
37 L. Foppa, K. Yamamoto, W.-C. Liao, A. Comas-Vives and C. Copéret, *J. Phys. Chem. Lett.*, 2018, **9**, 3348–3353.
38 J. Autschbach, S. Zheng and R. W. Schurko, *Concepts Magn. Reson., Part A*, 2010, **36A**, 84–126.
39 L. L. G. Justino, M. L. Ramos, F. Nogueira, A. J. F. N. Sobral, C. F. G. C. Geraldes, M. Kaupp, H. D. Burrows, C. Fiolhais and V. M. S. Gil, *Inorg. Chem.*, 2008, **47**, 7317–7326.
40 L. L. G. Justino, M. L. Ramos, M. Kaupp, H. D. Burrows, C. Fiolhais and V. M. S. Gil, *Dalton Trans.*, 2009, **0**, 9735–9745.
41 E. Lam, A. Comas-Vives and C. Copéret, *J. Phys. Chem. C*, 2017, **121**, 19946–19957.
42 E. Lam and C. Copéret, *Helv. Chim. Acta*, 2018, **101**, e1800120.
43 M. Leskes, N. E. Drewett, L. J. Hardwick, P. G. Bruce, G. R. Goward and C. P. Grey, *Angew. Chem., Int. Ed.*, 2012, **51**, 8560–8563.
44 J. Lu, X. Kong, V. Terskikh and G. Wu, *J. Phys. Chem. A*, 2015, **119**, 8133–8138.
45 S. Zhang, M. J. Nava, G. K. Chow, N. Lopez, G. Wu, D. R. Britt, D. G. Nocera and C. C. Cummins, *Chem. Sci.*, 2017, **8**, 6117–6122.
46 R. Gupta, J. Stringer, J. Struppe, D. Rehder and T. Polenova, *Solid State Nucl. Magn. Reson.*, 2018, **91**, 15–20.
47 C. M. Widdifield and R. W. Schurko, *Concepts Magn. Reson., Part A*, 2009, **34A**, 91–123.
48 J. Zhu, T. Kurahashi, H. Fujii and G. Wu, *Chem. Sci.*, 2012, **3**, 391–397.
49 R. N. Kerber, A. Kermagoret, E. Callens, P. Florian, D. Massiot, A. Lesage, C. Copéret, F. Delbecq, X. Rozanska and P. Sautet, *J. Am. Chem. Soc.*, 2012, **134**, 6767–6775.
50 R. N. Kerber, T. Kerber, X. Rozanska, F. Delbecq and P. Sautet, *Phys. Chem. Chem. Phys.*, 2015, **17**, 26937–26945.
51 D. Culver, W. Huynh, H. Tafazolian, T.-C. Ong and M. Conley, *Angew. Chem., Int. Ed.*, 2018, **57**, 9520–9523.
52 K. Yamamoto, S. Tanaka, H. Hosoya, H. Tsurugi, K. Mashima and C. Copéret, *Helv. Chim. Acta*, DOI: 10.1002/hlca.201800156.
53 S. E. Ashbrook and M. E. Smith, *Chem. Soc. Rev.*, 2006, **35**, 718–735.
54 S. E. Ashbrook, *Phys. Chem. Chem. Phys.*, 2009, **11**, 6892–6905.
55 K. Yamada, in *Annual Reports on NMR Spectroscopy*, ed. G. Webb, Academic Press, 2010, vol. 70, pp. 115–158.
56 J. J. Barieux and J. P. Schirmann, *Tetrahedron Lett.*, 1987, **28**, 6443–6446.
57 J. K. Crandall and M. A. Centeno, *J. Org. Chem.*, 1979, **44**, 1183–1184.
58 L. Antolini, R. Benassi, S. Ghelli, U. Folli, S. Sbardellati and F. Taddei, *J. Chem. Soc., Perkin Trans. 1*, 1992, **0**, 1907–1913.
59 L. Cassidei, M. Fiorentino, R. Mello, O. Sciacovelli and R. Curci, *J. Org. Chem.*, 1987, **52**, 699–700.
60 G. Schreckenbach and T. Ziegler, *J. Phys. Chem.*, 1995, **99**, 606–611.
61 J. A. Bohmann, F. Weinhold and T. C. Farrar, *J. Chem. Phys.*, 1997, **107**, 1173–1184.
62 E. L. Sceats, J. S. Figueroa, C. C. Cummins, N. M. Loening, P. Van der Wel and R. G. Griffin, *Polyhedron*, 2004, **23**, 2751–2768.
63 J. Autschbach, *J. Chem. Phys.*, 2008, **128**, 164112.
64 M. Pascual-Borras, X. Lopez, A. Rodriguez-Fortea, R. J. Errington and J. M. Poblet, *Chem. Sci.*, 2014, **5**, 2031–2042.
65 I. B. Moroz, K. Larmier, W.-C. Liao and C. Copéret, *J. Phys. Chem. C*, 2018, **122**, 10871–10882.
66 A. D. Walsh, *Trans. Faraday Soc.*, 1949, **45**, 179–190.
67 E. D. Glendening, J. K. Badenhoop, A. E. Reed, J. E. Carpenter, J. A. Bohmann, C. M. Morales, C. R. Landis and F. Weinhold, *NBO 6.0*, University of Wisconsin, Madison, 2013.

68 M. S. Reynolds and A. Butler, *Inorg. Chem.*, 1996, **35**, 2378–2383.
69 A. M. Al-Ajlouni and J. H. Espenson, *J. Org. Chem.*, 1996, **61**, 3969–3976.
70 S. A. Hauser, V. Korinth, E. Herdtweck, M. Cokoja, W. A. Herrmann and F. E. Kühn, *Eur. J. Inorg. Chem.*, 2010, 4083–4090.
71 P. Gisdakis, S. Antonczak, S. Küstlmeier, W. A. Herrmann and N. Rösch, *Angew. Chem., Int. Ed.*, 1998, **37**, 2211–2214.
72 W.-D. Wang and J. H. Espenson, *J. Am. Chem. Soc.*, 1998, **120**, 11335–11341.
73 M. Kaupp, O. L. Malkina and V. G. Malkin, *J. Chem. Phys.*, 1997, **106**, 9201–9212.
74 W. A. Herrmann, H. Ding, F. E. Kühn and W. Scherer, *Organometallics*, 1998, **17**, 2751–2757.
75 A. M. Al-Ajlouni and J. H. Espenson, *J. Am. Chem. Soc.*, 1995, **117**, 9243–9250.
76 D. J. Berrisford, C. Bolm and K. B. Sharpless, *Angew. Chem., Int. Ed. Engl.*, 1995, **34**, 1059–1070.
77 A. K. Rappé and W. A. Goddard III, *Nature*, 1980, **285**, 311.
78 A. K. Rappé and W. A. Goddard III, *J. Am. Chem. Soc.*, 1982, **104**, 448–456.
79 J. M. Gonzales, R. Distasio, R. A. Periana, W. A. Goddard and J. Oxgaard, *J. Am. Chem. Soc.*, 2007, **129**, 15794–15804.